Absolute cross sections and asymmetry parameters for photodetachment of C⁻(⁴Sᵒ)

Raphaël Marion,[1] Kevin M. Dunseath,[2] Mariko Terao-Dunseath,[2] and Xavier Urbain ●[1,*]

[1]*Institute of Condensed Matter and Nanosciences, Université Catholique de Louvain, Louvain-la-Neuve B-1348, Belgium*
[2]*Univ Rennes, CNRS, IPR (Institut de Physique de Rennes)–UMR 6251, F-35000 Rennes, France*

Absolute total cross sections and asymmetry parameters for the photodetachment of the ⁴Sᵒ ground state of C⁻ are reported for photon energies ranging from threshold to 6 eV. The total cross sections were measured using the animated crossed beam technique incorporating corrections for saturation, while the asymmetry parameters were obtained using velocity map imaging spectrometry. The measured values are in good agreement with theoretical results obtained from an *R*-matrix calculation using polarized pseudostates.

I. INTRODUCTION

The study of the photodetachment of negative ions, especially of open-shell systems such as carbon and oxygen, presents a double interest: they play an important role in astrophysics and atmospheric physics [1], and provide stringent tests for the description of electron correlation. The electron affinity, or energy difference between the ground states of the negative ion and the residual atom, is indeed much smaller than the ionization energy of atoms and cations. While the variational principle applies *independently* for each system, it is much more difficult to guarantee a well-balanced calculation for *both* systems, and hence an accurate value for the electron affinity.

A comprehensive review of the knowledge of the structure and dynamics of atomic anions has been compiled by Andersen [2], who focused in particular on the decade between 1994 and 2004. In the case of O⁻, there was a long-standing discrepancy between experiment and theory, which was only recently resolved by new measurements using the animated crossed beam technique to determine absolute total cross sections [3]. These are about 17% larger than the earlier data, and are in very good agreement with the theoretical results presented in the same publication. Since the most extensive set of experimental near-threshold photodetachment cross sections for C⁻(⁴Sᵒ) dates back to 1962 and was normalized using the earlier data for O⁻ [4], a direct measurement appears timely.

The carbon anion exists in two bound states: the ground state C⁻($1s^2 2s^2 2p^3\ ^4S^o$), which has an affinity of 1.262 122 6(11) eV with respect to the C($1s^2 2s^2 2p^2\ ^3P_0$) ground level [5], and an excited state C⁻($1s^2 2s^2 2p^3\ ^2D^o$) which is very weakly bound by about 33 meV [6]. In this work, we consider only photodetachment from the ⁴Sᵒ ground state. At low energy, this results in the ejection of a $2p$ bound electron into the s or d wave, leaving the residual atom in its ground state:

$$\mathrm{C}^-(1s^2 2s^2 2p^3\ ^4S^o) + \gamma \rightarrow \mathrm{C}(1s^2 2s^2 2p^2\ ^3P) + e^-\ (\ell = 0, 2).$$

Above 4 eV, it becomes possible to leave the residual atom in its first spin-allowed excited state, C($1s^2 2s 2p^3\ ^5S^o$), while

ejecting a p-wave photoelectron:

$$\mathrm{C}^-(1s^2 2s^2 2p^3\ ^4S^o) + \gamma \rightarrow \mathrm{C}(1s^2 2s 2p^3\ ^5S^o) + e^-\ (\ell = 1).$$

As the photon energy increases, more final excited states of the residual atom become accessible. In work published just after the review by Andersen [2], Zhou *et al.* [7] computed the photodetachment cross section up to 13 eV, including the excitation of the residual atom up to the C($1s^2 2s 2p^3\ ^5P^o$) state. At yet higher photon energies, core-hole ionization opens up and multiple photodetachment of C⁻ takes place, as studied by Gibson *et al.* [8], and more recently, in the comprehensive work on inner-shell photodetachment conducted by Perry-Sassmannshausen *et al.* [9].

The structure of the paper is as follows: the experimental method used to determine the absolute cross sections and the asymmetry parameter β for photodetachment is described in Sec. II; Sec. III explains how carbon wave functions were optimized in view of *ab initio R*-matrix calculations; results and comparison with previous data are detailed in Sec. IV. The conclusions and perspectives for future work are presented in Sec. V.

II. EXPERIMENT

Our experimental method has been presented in detail in previous publications [3,10,11]. We will therefore only describe the main features of the different techniques used in the current work, in particular the approach used to determine corrections for saturation effects when using pulsed lasers.

A. Experimental setup

The experimental setup can operate in two independent modes and is shown schematically in Fig. 1. The atomic beam is produced by a duoplasmatron source filled with CO_2 gas, at a potential of 4 kV. A permanent magnet performs a mass selection and the cleaned and collimated beam (diameter 1 mm) is then bunched by an electrostatic deflector in front of an aperture to limit detector aging. After interaction, residual anions are collected in a Faraday cup in order to measure the current I_0, which is typically 100 pA. Continuous light sources are provided by different solid-state lasers at 778, 532, and
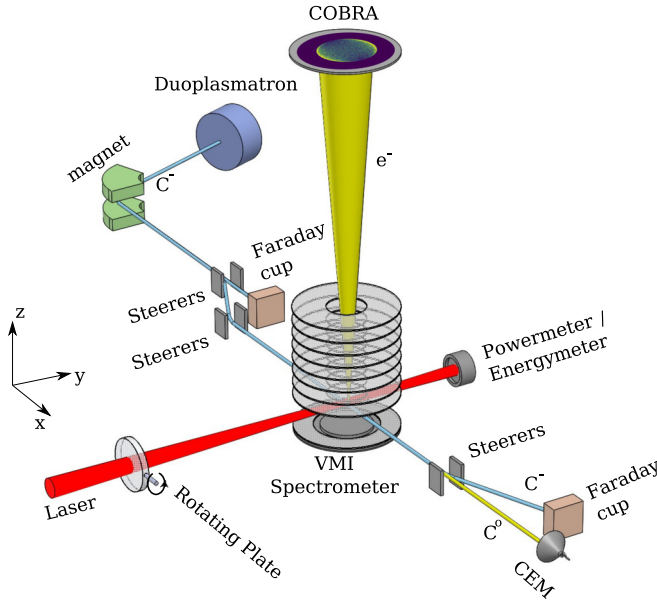
*xavier.urbain@uclouvain.be

FIG. 1. Experimental setup.

405 nm wavelengths. The pulsed light source is from an OPO laser system (NT342A-30 from Ekspla), tunable from 2600 to 225 nm, with a repetition rate of 30 Hz. Photon energies up to 6 eV are reached using an external beta barium borate (BBO) crystal.

In the first mode, based on the animated crossed beam technique, a polarizing beam splitter combined with a half-wave plate selects the horizontal polarization and tunes the energy of the laser pulses. The animation of the laser beam is carried out by rotating a 12-mm-thick antireflection coated plate whose axis lies perpendicular to the laser beam propagation axis. The pulse energy, tuned to about 20 μJ, is measured by a Thorlabs ES111C pyroelectric energy sensor while the continuous power is measured by a Thorlabs S310C thermal power sensor and varied between 40 and 100 mW depending on the solid-state laser. During experiments with continuous light, the anion beam current is also continuous while with pulsed light, the anions are bunched at 30 Hz in 3.3 ms packets. In the interaction zone, the anion and photon beams cross at right angles. The neutrals follow a straight trajectory and are counted with a channel electron multiplier (CEM; KBL 25RS from Sjuts Optotechnik) with a high detection efficiency. The anion beam is deflected by an electrostatic field and the current is measured with a Faraday cup.

In the second mode, the VMI spectrometer is turned on while working at a higher pulse energy (250 μJ) with much shorter anion packets (1 μs) in order to increase the signal-to-noise ratio (SNR). The photoelectrons are extracted perpendicularly by an electrostatic plate and directed to the electrostatic lens designed following [12]. The repeller electrode is split to correct the trajectory of the anions as explained in [13]. Photoelectrons are detected using a COBRA system [14], comprising three stacked microchannel plates (MCPs), a phosphor screen, a complementary metal-oxide semiconductor (CMOS) camera, and a waveform digitizer.

Data acquisition as well as fast digital control are achieved using a field-programmable gate array (FPGA) board while the whole setup is supervised by a LabVIEW application.

B. Absolute cross-section measurements

1. The ACB technique

The absolute measurement of the cross section is based on the animated crossed beam (ACB) technique [10], in which the laser beam is periodically swept through the perpendicular anion beam. The laser is characterized by its frequency ω, pulse duration T_p, and, in a reference frame whose origin is fixed at the beam intersection in the center of the interaction zone, by the flux density of photons $\phi_p(x, y, z - Z, t)$ in the direction of propagation. Z is the offset of the laser beam as it is swept across the anion beam. The normalized photon flux density, $\hat{\phi}(x, y, z, t)$, is assumed to be constant from pulse to pulse while the energy $E_{p,Z}$ may substantially vary for each pulse p of the n_Z laser shots (typically 120 for good statistics) carried out at each offset Z:

$$\phi_p(x, y, z - Z, t) = \frac{E_{p,Z}}{\hbar\omega}\hat{\phi}(x, y, z - Z, t).$$

The C$^-$ anions, produced in a duoplasmatron source with a bias potential $-V_S$, have a nominal velocity $v = \sqrt{2eV_S/M_{C^-}}$, where M_{C^-} is the mass of C$^-$ and e is the elementary charge. At any instant during pulse p, as the velocity $v \ll c$, the laser illuminates an almost static distribution of anions $\rho(x, y, z, t)$, governed by the equation

$$\vec{\nabla} \cdot \vec{j} + \frac{\partial\rho}{\partial t} = -\sigma\phi\rho,$$

where $\vec{j} = \rho\vec{v}$ is the anion current density and σ the photodetachment cross section. The solution of this equation for the pulse starting at $t = t_{p,Z}$ is formally given by

$$\rho_p(x, y, z, t; Z) = \rho(x, y, z; t_{p,Z})\exp\left\{-\sigma\int_{-\infty}^{x}\frac{dx'}{v}\phi_p(x', y, z - Z, t - \frac{x - x'}{v})\right\}.$$

The initial distribution of anions, $\rho(x, y, z; t_{p,Z})$, can be factorized into a normalized distribution $\hat{\rho}(x, y, z)$ valid for all pulses and a fluctuating magnitude related to the total current $I_{p,Z} = \iint e\rho v\, dy\, dz$ delivered by the source to the entrance of the interaction zone at the time of the laser shot:

$$\rho(x, y, z; t_{p,Z}) = \frac{I_{p,Z}}{ev}\hat{\rho}(x, y, z).$$

For a detector of neutrals located at a position x_d far after the interaction zone, with an efficiency η and an active surface S_d larger than the cross-sectional area of the anion beam, we can express the count of neutrals for a pulse p as

$$N_{p,Z} = \eta\int dt\iint_{S_d} dy\, dz\, v\rho(x_d, y, z; t_{p,Z})\left[1 - \exp\left\{-\sigma\int_{-\infty}^{x_d}\frac{dx'}{v}\phi_p\left(x', y, z - Z, t - \frac{x_d - x'}{v}\right)\right\}\right]. \tag{1}$$

If the argument of the exponential in Eq. (1) is small enough so that a first-order expansion is sufficient, the neutral count $N_{p,Z}$ is proportional to the cross section σ. After normalizing $N_{p,Z}$ with respect to the current $I_{p,Z}$ and energy $E_{p,Z}$ and integrating over all laser offsets Z, the remaining integrals involve only $\hat{\phi}$ and $\hat{\rho}$, which result in a constant scale factor whose determination does not require any further assumptions about the beam profiles.

We obtain the ACB expression for the photodetachment cross section:

$$\sigma_{\text{pulsed}}^{\text{ACB}} = \frac{1}{\eta} \sum_Z \frac{\Delta Z}{n_Z} \sum_{p=1}^{n_Z} \frac{\hbar\omega}{E_{p,Z}} \frac{ev}{I_{p,Z}} N_{p,Z}. \qquad (2)$$

This highlights the major advantage of the ACB technique; the experimental cross section does not depend on the geometrical overlap of the beams, which is critical and difficult to measure accurately in standard beam-beam interaction experiments.

For continuous lasers, the integration over pulse duration is irrelevant and the production rate R_Z of neutrals is directly measured by the CEM and normalized to the power P_Z of the laser beam at position Z instead of the pulse energy $E_{p,Z}$, and to the anion current I_Z:

$$\sigma_{\text{cont}}^{\text{ACB}} = \frac{1}{\eta} \sum_Z \Delta Z \frac{\hbar\omega}{P_Z} \frac{ev}{I_Z} R_Z. \qquad (3)$$

2. Saturation effects from a pulsed laser

The ACB technique has been successfully implemented and used to determine absolute cross sections for many electron-ion [15–17] and electron-atom [18,19] interactions as well as for the photodetachment of H^- [20] and O^- [3,11]. The few necessary assumptions that are satisfied in the case of continuous lasers, however, do not always hold for pulsed lasers: as the peak intensity may become high even for pulses of relatively low energy, the first-order approximation for the exponential function appearing in Eq. (1) may be no longer valid, particularly in the infrared domain or when the cross section becomes large. Higher order terms in the expansion of the exponential in Eq. (1) contribute an extra term s_p representing the phenomenon of saturation:

$$\int dt \sum_Z \frac{\hbar\omega}{E_{p,Z}} \left[1 - \exp\left\{ -\sigma \int_{-\infty}^{x_d} \frac{dx'}{v} \phi_p \right\} \right] \equiv \frac{\sigma}{v}[1 - s_p(\sigma)].$$

Inserting this in Eq. (2) yields a self-consistent expression for σ which must be solved by iteration, starting from $\sigma_0 = \sigma^{\text{ACB}}$, until a stationary value of the cross section is reached:

$$\sigma_{i+1} = \frac{\sigma^{\text{ACB}}}{1 - s(\sigma_i)}, \qquad (4)$$

where $s(\sigma)$ is the correction for saturation averaged over the n_Z laser pulses, taking into account the fluctuations of energy shown in Fig. 2.

Unfortunately, assumptions concerning the beam profiles are now unavoidable. Provided that the Rayleigh length is greater than the diameter of the circular anion beam, which has a waist $w_0 \in [250, 300]$ μm and a pulse duration $T_p \in [7, 9]$ ns, we can expand the laser profile about the coordinates
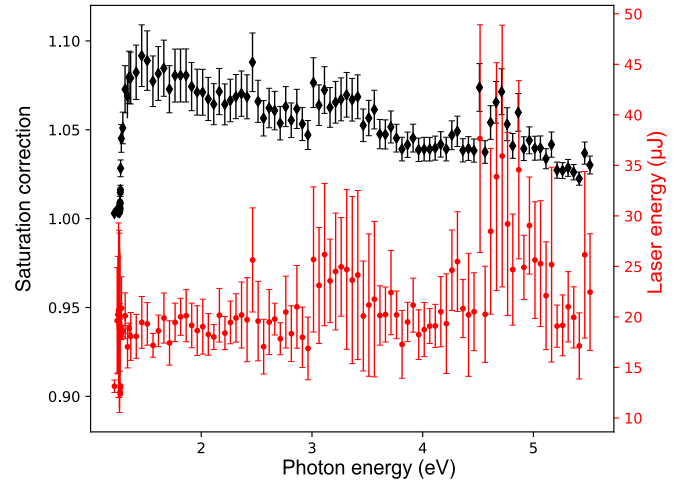

FIG. 2. Correction of saturation for the cross section at each wavelength, and fluctuations of the pulse energy of the laser. Full lozenge: correction of saturation; full circle: pulse energy.

of its maximum t_M $(-T_p/2 \leqslant t - t_M \leqslant T_p/2)$ as

$$\hat{\phi}(x, y, z, t) = \frac{2}{T_p} \frac{2}{\pi w_0^2} \cos^2\left(\pi \frac{t - t_M}{T_p}\right) \exp\left\{-2 \frac{x^2 + z^2}{w_0^2}\right\}. \qquad (5)$$

The factor by which σ^{ACB} must be multiplied to correct for saturation effects is shown in Fig. 2. Its effect is to slightly increase the apparent cross section, particularly at lower photon energies. Since assumptions concerning the beam profiles are needed to estimate the saturation correction, it may seem that the main advantage of the ACB technique is somehow lost. The corrections, however, remain small and the whole procedure can be validated by comparison with measurements using a continuous laser, which is not subject to saturation, or obtained with a pulsed laser at lower energy and/or higher frequency, as will be shown in Sec. IV.

C. Differential cross-section measurements

In the case of detachment by linearly polarized light, in the dipole approximation, additional information provided by the angular distribution of photoelectrons can be conveniently summarized using the asymmetry parameter β,

$$\frac{d\sigma}{d\Omega} = \frac{\sigma}{4\pi}[1 + \beta P_2(\cos\theta)], \qquad (6)$$

relating the differential cross section $d\sigma/d\Omega$ to the total cross section σ, where P_2 is the second-order Legendre polynomial and θ is the angle between the photoelectron momentum and the laser polarization axis. The parameter β can be measured by means of a velocity map imaging (VMI) spectrometer: photodetachment occurs inside an electric field perpendicular to both the anion beam and the direction of the laser polarization. This electric field slightly bends the trajectory of the anion beam while totally separating out the less energetic photoelectrons. Following [21], this almost perpendicular photoelectron beam is then guided through a thick electrostatic lens formed by stacking biased circular electrodes whose voltages have been optimized by simulation

in order to achieve the best resolution. The position sensitive detector is placed at the focal plane where the image formed is the Fourier transform of the transverse momentum of the photoelectron cloud which, in the absence of aberrations, is independent of the location where photodetachment took place.

Outside the lens, the velocity of the photoelectrons depends on the kinetic energy release (KER) of the photodetachment channel and on the bias potential applied to the repeller electrode. The photoelectrons therefore travel on expanding Newton spheres that are projected onto the detector screen. Assuming an azimuthal symmetry, it is possible to reconstruct from the two-dimensional image the three-dimensional angular distribution of the photoelectrons by an inverse Abel transform, for which many computational techniques are available. In this work, we use the MEVELER algorithm based on a Bayesian approach, developed in [22].

D. Analysis of experimental uncertainties

1. Absolute cross sections

By detecting both products of the photodetachment in coincidence, the efficiency η of the CEM can be estimated. Using the logical conjunction symbol $\wedge$, we denote by $(e \wedge l)$ the detection of a photoelectron in coincidence with a laser pulse, and by $(n \wedge e \wedge l)$ the simultaneous detection of a neutral. Provided all the detected electrons are produced by photodetachment, the binomial statistical estimate of η and its variance are

$$\hat{\eta} = \frac{\#(n \wedge e \wedge l)}{\#(e \wedge l)};$$

$$\mathrm{Var}[\hat{\eta}] = \frac{\hat{\eta}(1 - \hat{\eta})}{\#(e \wedge l)},$$

where the symbol # stands for the number of coincidences of a given type. This estimate can be used to calibrate new detectors or to compensate for aging, with an accuracy of about 1%, depending on the number of events. For the present experiment we have observed a quite stable value of $\eta = 95 \pm 0.5\%$ during the whole process. To test the method, we have analyzed the efficiency of another CEM detector, older and smaller, and obtained a value of $\eta = 90 \pm 1\%$.

In ACB measurements with pulsed lasers, two or more events detected during the same laser-neutral coincidence time window will be counted as one. Under normal conditions, with a weak anion current and low photodetachment rates, the probability of such a counting loss is small. We expect the number m_p of neutrals effectively produced in a pulse to follow Poisson statistics, characterized by a mean value $\hat{m}$:

$$P[m_p|\hat{m}] = \frac{\hat{m}^{m_p}}{m_p!} \exp(-\hat{m}),$$

and the number of detected neutrals m_d to follow binomial statistics:

$$P[m_d = y \,|\, \eta, m_p] = \binom{m_p}{y} \eta^y (1 - \eta)^{m_p - y}.$$

The value of $\hat{m}$ may be deduced from the total number m_T of counted neutrals for n pulses by noting that the apparent rate per pulse $\bar{m} = m_T/n$ ($\bar{m} < 1$) is the complement of the probability of no detection, yielding the relation

$$\bar{m} = P[m_d \geqslant 1] = 1 - P[m_d = 0]$$

$$= 1 - \sum_{m_p} P[m_d = 0 \,|\, \eta, m_p] P[m_p|\hat{m}]$$

$$\implies \bar{m} = 1 - e^{-\eta\hat{m}}.$$

In the following, the quantity $\eta\hat{m}$ will be denoted by $\hat{m}_d$.

The background contribution to $\hat{m}_d$ is estimated by duplicating the coincidence time window with an arbitrary delay and applying the same Poisson correction to the total number b_T of neutrals detected out of coincidence during the same n_Z pulses. With these definitions, the mean rate and variance for neutral detection per pulse $\hat{N}_Z$ entering Eq. (2) is given by

$$\hat{N}_Z = \hat{m}_{d,Z} - \hat{b}_{d,Z};$$

$$\mathrm{Var}[\hat{N}_Z] = \frac{\hat{m}_{d,Z} + \hat{b}_{d,Z}}{n_Z}$$

with $\hat{m}_{d,Z} = -\ln(1 - \bar{m}_Z)$ and $\hat{b}_{d,Z} = -\ln(1 - \bar{b}_Z)$.

For continuous light, we have improved the estimate of the background compared to our previous setup [3] by implementing a mechanical shutter to measure alternatively the signal and the background n_s times at each offset Z of the laser beam during the whole sweep time, rather than only at the beginning and at the end of each experimental run. With a switching delay T_s leading to durations of direct and background measurements $T_m = T_b = n_s T_s$, during which m_T and b_T neutrals are respectively counted, the detection rate $\hat{R}_Z$ entering Eq. (3) is estimated by

$$\hat{R}_Z = \hat{R}_{m,Z} - \hat{R}_{b,Z};$$

$$\mathrm{Var}[\hat{R}_Z] = \frac{\hat{R}_{m,Z} + \hat{R}_{b,Z}}{n_s T_s},$$

with $\hat{R}_{m,Z} = m_{T,Z}/T_m$ and $\hat{R}_{b,Z} = b_{T,Z}/T_b$.

The contribution of the variance of the signal to the variance of the experimental cross section is given by

$$\mathrm{Var}[\hat{\sigma}_{\mathrm{pulsed}}] = \sum_{p,Z} \left(\frac{1}{n_Z} \frac{\Delta Z}{\eta} \frac{\hbar\omega}{E_{p,Z}} \frac{\mathrm{ev}}{I_{p,Z}} \right)^2 \mathrm{Var}[\hat{N}_{p,Z}],$$

$$\mathrm{Var}[\hat{\sigma}_{\mathrm{cont}}] = \sum_Z \left(\frac{\Delta Z}{\eta} \frac{\hbar\omega}{P_Z} \frac{\mathrm{ev}}{I_Z} \right)^2 \mathrm{Var}[\hat{R}_Z].$$

Sufficient internal statistical precision is usually obtained by one Z scan for a continuous laser and by five Z scans for pulsed light.

A final source of uncertainties arises from the observed fluctuations of measured cross sections over different runs, which might be due to variations of spatial distributions, especially in the laser beam. Fortunately, these variations average to zero so that increasing the number of runs (a repeatability test) is sufficient to improve the external statistics and reach the objective of 2% uncertainty for a pulsed laser and 0.5% for a continuous laser. The final values are obtained by calculating

TABLE I. Typical values for experimental uncertainties using the ACB technique.

Uncertainties type A (statistical):	
Detector efficiency	0.5%
Correction for saturation	1%
Statistical uncertainties with pulsed laser	2%
Statistical uncertainties with CW laser	0.5%
Combined uncertainties type A:	
Pulsed laser	2.3%
CW laser	0.7%
Uncertainties type B (systematic):	
Power meter/Energy meter	3.1%
Resolution	0.5%
Calibration	3%
Electrometer	1.1%
Resolution	0.5%
Calibration	1%
Vertical displacement Z	2%
Combined uncertainties type B:	3.8%
Final combined uncertainties:	
Pulsed laser	4.5%
Continuous laser	3.9%

the weighted average over several runs:

$$\hat{\sigma}_{\text{pulsed}}^{\text{ACB}} = \sum_j \frac{\hat{\sigma}_j}{\text{Var}[\hat{\sigma}_j]} \bigg/ \sum_j \frac{1}{\text{Var}[\hat{\sigma}_j]}; \tag{7}$$

$$\text{Var}\big[\hat{\sigma}_{\text{pulsed}}^{\text{ACB}}\big] = 1 \bigg/ \sum_j \frac{1}{\text{Var}[\hat{\sigma}_j]}. \tag{8}$$

A summary of typical uncertainty values is presented in Table I, following [23] for the classifications and rules for combining experimental uncertainties.

2. Asymmetry parameters

To the best of our knowledge, there are no reliable statistical estimators for asymmetry parameters. Here we propose one such estimator for N events.

We start from a general probability distribution in spherical coordinates with azimuthal symmetry:

$$P(v, \theta, \phi) = \frac{p(v)}{4\pi v^2} \left(\sum_{\ell=0}^{L} \beta_\ell P_\ell(\cos\theta) \right), \tag{9}$$

normalized so that

$$\int_0^\infty \int_0^\pi \int_0^{2\pi} dv \, d\theta \, d\phi \, v^2 \sin\theta \, P(v, \theta, \phi) = 1,$$

where $p(v)$ is the radial velocity distribution normalized so that $\int p(v) dv = 1$ and P_ℓ is the Legendre polynomial of degree ℓ. The coefficients β_ℓ are then given by

$$\beta_\ell = (2\ell + 1) \int_0^\infty \int_0^\pi \int_0^{2\pi} dv \, d\theta \, d\phi \, v^2 \sin\theta$$
$$\times P_\ell(\cos\theta) P(v, \theta, \phi). \tag{10}$$

The right-hand side of this equation can be interpreted as the expectation value $E[X^{[\ell]}]$ of $X^{[\ell]} = (2\ell + 1) P_\ell(\cos\theta)$ with

respect to the probability distribution $P(v, \theta, \phi)$. We can also define the variance of $X^{[\ell]}$ as

$$\text{Var}[X^{[\ell]}] = E[(X^{[\ell]})^2] - \big(E[X^{[\ell]}]\big)^2$$

$$= (2\ell + 1)^2 \sum_{\ell'=0}^{L} \begin{pmatrix} \ell & \ell & \ell' \\ 0 & 0 & 0 \end{pmatrix}^2 \beta_{\ell'} - \beta_\ell^2. \tag{11}$$

We now consider an experiment providing N independent observations θ_i, $i \in \{1, \ldots, N\}$, of the polar angle θ. The sample mean

$$\hat{\beta}_\ell = \frac{1}{N} \sum_{i=1}^{N} X_i^{[\ell]} = \frac{2l + 1}{N} \sum_{i=1}^{N} P_l(\cos\theta_i), \tag{12}$$

is then an unbiased estimator which, following the central limit theorem, converges to β_ℓ as $N \to \infty$. The experimental variance for large sample sizes is $\text{Var}[X^{[\ell]}]/N$, which vanishes as $N \to \infty$ so that the estimator is consistent. We note that the presence of the Wigner 3-j symbol in Eq. (11) implies that the precision of $\hat{\beta}_\ell$ is blurred by all the even distributions $P_{\ell'}(\cos\theta)$ with ℓ' even between 0 and 2ℓ.

In the specific case of photodetachment by linearly polarized light, the dipole selection rules lead to the expression (6) for the differential cross section, which involves only $\ell = 0$ and 2. Since $\beta_0 = 1$, β_2 is known as the asymmetry parameter commonly denoted β. For the same reasons, the upper limit of the summations over ℓ or ℓ' in Eqs. (9) and (11) is $L = 2$. The statistical precision for the estimation of β, from Eq. (11) with $\ell = 2$, only contains contributions from $\ell' = 0$ and 2, leading to

$$\frac{5}{N} + \frac{10\hat{\beta}}{7N} - \frac{\hat{\beta}^2}{N}. \tag{13}$$

These results, however, cannot be directly applied to our data since the spherical distribution itself is not known experimentally, only its projection. The Abel inversion provided by the maximum entropy (MAXENT) approach [22] gives an estimate of the distribution in an unnormalized form:

$$\mathcal{P}(v, \theta, \phi) = \frac{1}{4\pi v^2} [Q_0(v) + Q_2(v) P_2(\cos\theta)]. \tag{14}$$

Integrating Eq. (14) over the velocity space gives the total number of events $N = \int Q_0(v) dv$, while direct comparison with Eq. (9) yields an estimate $\hat{\beta}(v) = Q_2(v)/Q_0(v)$. The dependency of $\hat{\beta}$ on v, which arises from the unavoidable dispersion associated with the limited precision of the experimental setup, prevents a direct determination of the best and unique value of the asymmetry parameter and its precision from $Q_0(v)$ and $Q_2(v)$, even for cases with a single detachment channel.

Following Eq. (10), we define the experimental estimate of $\hat{\beta}$ as the expectation value of $X^{[2]}$ with respect to the probability distribution (14) normalized by the factor $1/N$:

$$\hat{\beta} = E[5 P_2(\cos\theta)]$$

$$= \frac{5}{N} \int_0^\infty \int_0^\pi \int_0^{2\pi} dv \, d\theta \, d\phi \, v^2 \sin\theta P_2(\cos\theta) \mathcal{P}(v, \theta, \phi),$$

TABLE II. Typical values for experimental uncertainties in the asymmetry parameters.

Systematic errors:	
Circularization and Abel inversion	$\Delta\beta = 0.01$
Background filtering	$\Delta\beta = 0.01$
Statistical uncertainties:	$\Delta\beta = 0.007$

which yields

$$\hat{\beta} = \frac{1}{N}\int Q_2(v)dv = \frac{\int Q_2(v)dv}{\int Q_0(v)dv}. \tag{15}$$

In practice, the definition of the limits of the integrals over v requires some prior information about the physical process in order to define, for example, the number of peaks expected and their energy range. In this work, where all the peaks are clearly identified, we select the range Δv of v such that $Q_0(v)$ is greater than 10% of the local maximum. The number of events, $\int_{\Delta v} Q_0(v)dv$, is of the order of 10^5, leading to an uncertainty, given by Eq. (13), of $\Delta\hat{\beta} \approx 0.007$. To these statistical uncertainties, we add an absolute error $\Delta\beta = 0.01$ to take into account the systematic errors of circularization of the data and the internal uncertainties arising from the MEVELER algorithm. For photon energies larger than 3.4 eV, where background noise starts to appear, we include an additional $\Delta\beta = 0.01$ in the absolute error to account for filtering in the background procedure. Above 4 eV, the increasingly large background noise renders the filtering procedure less effective and the parameter β becomes inaccessible.

Typical values for experimental uncertainties in the asymmetry parameters are summarized in Table II.

III. THEORY

Photodetachment cross sections and asymmetry parameters were calculated using standard, nonrelativistic R-matrix theory as implemented in the UK APAP (Atomic Processes for Astrophysical Plasmas) suite of computer codes [24]. In this approach, initially developed in order to study resonances in nucleon-nucleus collisions [25], configuration space is naturally divided into two parts: the inner region, where all $(N+1)$ electrons interact strongly and the solution is expanded in a basis of discrete functions analogous to bound states in a finite box, built using a set of N-electron target wave functions coupled to R-matrix continuum orbitals describing the projectile electron; and the outer region, where the solution can be written as the simple product of target and projectile wave functions. In atomic physics, all potentials are known but long-range couplings in the outer region must be fully taken into account. The collisional approach can be extended to photoionization and photodetachment by considering these processes as half-collisions: the asymptotically vanishing initial bound state is the solution of the close-coupling problem with all channels closed. Such a solution only exists for a negative energy that must be found numerically by an iterative approach. In the weak field regime considered here, the photodetachment cross section can be evaluated using perturbation theory: it is proportional to the

TABLE III. Parameters of the ten Slater orbitals optimized on the energy and polarizability of the $C(1s^2 2s^2 2p^2\ ^3P)$ ground state using the computer code CIVPOL [28].

	$C_{jn\ell}$	$I_{jn\ell}$	$\zeta_{jn\ell}$		$C_{jn\ell}$	$I_{jn\ell}$	$\zeta_{jn\ell}$
$1s$	23.64032	1	5.43599	$2p$	0.31061	2	0.98073
	4.04776	1	9.48256		1.58145	2	1.44361
	0.00110	2	1.05749		2.92085	2	2.60051
	-0.00583	2	1.52427		1.27982	2	6.51003
	0.07620	2	2.68435				
	0.15955	2	4.20096	$\bar{3}p$	5.75621	2	1.55007
					-2.37862	3	1.36859
$2s$	-5.27596	1	5.43599				
	-0.62547	1	9.48256	$\bar{4}p$	2.34572	2	0.51316
	0.10754	2	1.05749		-3.28476	3	0.68909
	2.48567	2	1.52427		1.03114	4	0.85291
	4.57346	2	2.68435				
	-6.16698	2	4.20096	$\bar{3}d$	3.94743	3	1.89468
$\bar{3}s$	6.92570	1	2.34033	$\bar{4}d$	2.78398	3	1.99721
	-20.83502	2	2.37260		-0.17968	4	1.07874
	2.68194	3	1.54022				
$\bar{4}s$	3.86042	1	1.25514	$\bar{4}f$	5.90852	4	2.41065
	-16.39226	2	1.23475				
	17.35377	3	1.61817				
	-0.05982	4	0.91968				

modulus square of the dipole matrix element between the initial bound state of C^- and a final continuum state of the neutral atom and an ejected photoelectron. This collisional wave function is determined at each photoelectron energy by matching at the boundary a the amplitude of the solutions of the inner and outer regions using the inverse log-derivative matrix. Full details of the R-matrix method are given in [26], in particular, Chapter 8 which treats photoionization.

In the spectral range covered by our experiment, we consider photodetachment of $C^-(1s^2 2s^2 2p^3\ ^4S^o)$, leaving the residual atom in one of the target states $C(1s^2 2s^2 2p^2\ ^3P)$ and $C(1s^2 2s 2p^3\ ^5S^o)$. The key point is to determine a set of atomic orbitals suitable, in a configuration interaction approach, for describing electron correlations in the inner region, delimited by the spatial extension of the most diffuse target state. The inner region therefore does not need to encompass the entire charge distribution of $C^-(1s^2 2s^2 2p^3\ ^4S^o)$. The orbitals must of course reproduce as accurately as possible not just the energy levels of the residual atom but also its electron affinity, which is very sensitive to the polarization of the target in the presence of the extra electron. The challenge is to optimize a finite set of orthonormal orbitals while taking into account all these physical effects.

In Table III, we present the parameters of the ten Slater-type orbitals chosen to describe carbon in our R-matrix calculations. The ^3P and $^5S^o$ configurations arising from the main configuration $1s^2 2s^2 2p^2$ with excitation of up to two electrons from the $n = 2$ shell are included in the basis and the respective Hamiltonian matrices are diagonalized. The spectroscopic $1s$, $2s$, and $2p$ orbitals are Hartree-Fock orbitals [27]. The other orbitals are optimized using the CIVPOL computer code [28]: $\bar{3}s$, $\bar{3}p$, $\bar{3}d$, and $\bar{4}f$ are optimized on the

TABLE IV. Energies of the $1s^2 2s^2 2p^2\ ^3P$ and $1s^2 2s 2p^3\ ^5S^o$ terms of carbon, together with those of the three polarized pseudostates included in the R-matrix calculations. The observed values are taken from the NIST Atomic Spectra Database [29].

	Absolute (a.u.)	Relative (eV)	Zhou et al. [7] (eV)	Observed (eV)
^3P	−37.77831	0.0	0.0	0.0
$^5S^o$	−37.62867	4.07191	3.97679	4.17895
$\overline{^3P^o}$	−37.40867	10.05842		
$\overline{^3D^o}$	−37.31503	12.60649		
$\overline{^3S^o}$	−37.26368	14.00380		

ground state energy of C(^3P), $\bar{4}s$, $\bar{4}p$ and $\bar{4}d$ are optimized on the ground state polarizability.

In Table IV, the energy of C($1s^2 2s^2 2p^2\ ^3P$) and C($1s^2 2s 2p^3\ ^5S^o$) are compared with the recommended values from NIST and those of an earlier calculation by Zhou et al. [7], who used a similar R-matrix approach combined with the variable phase method in the asymptotic region. The energy of the $^5S^o$ level with respect to that of the ground state differs by 2.6% from the observed value and can be considered as sufficiently good for the purpose of this work. The full average polarizability $\bar{\alpha}$ of C($1s^2 2s^2 2p^2\ ^3P$) obtained by including $\overline{^3S^o}$, $\overline{^3P^o}$, and $\overline{^3D^o}$ pseudostates is $11.58a_0^3$, close to the value of $11.67a_0^3$ from an extensive coupled cluster calculation [30].

The electron affinity of the carbon ground state is calculated using the program STGB in the UK APAP suite of codes [24]. This uses a perturbative treatment of the long-range potentials in the R-matrix outer region combined with an iterative search over negative energies to find bound state solutions for the $(N+1)$-electron system. The value of the electron affinity will thus depend on the size of the R-matrix inner region and the number of continuum orbitals used (a larger inner region requires more continuum orbitals to ensure convergence). In addition, we found that it was necessary to include excitation of at least two electrons from the $1s^2 2s^2 2p^3$ base configuration in order to obtain a bound state of C$^-$. For the results reported below, we in fact included excitation of up to three electrons. For an inner region size varying between $25a_0$ and $35a_0$ and the number of continuum orbitals between 25 and 50, we obtained values of the electron affinity ranging from 1.2575 to 1.2613 eV, which compare favorably with the value of 1.2658 eV corresponding to the energy difference between the weighted average of the experimental fine-structure levels of C(^3P) and the C$^-$($^4S^o$) ground state [5]. The electron affinity in the calculation by Zhou et al. [7] is 1.21 eV.

IV. RESULTS AND DISCUSSION

A. Total cross sections

The absolute cross sections for photodetachment of C$^-$($^4S^o$) from our experiment are presented in Fig. 3 and compared with those by Seman and Branscomb [4] and Haeffler et al. [31]. Other data in the threshold region by Feldmann [6], Hall and Siegel [32], and Brandon et al. [33] are not reproduced here as they are not absolute and cover a very
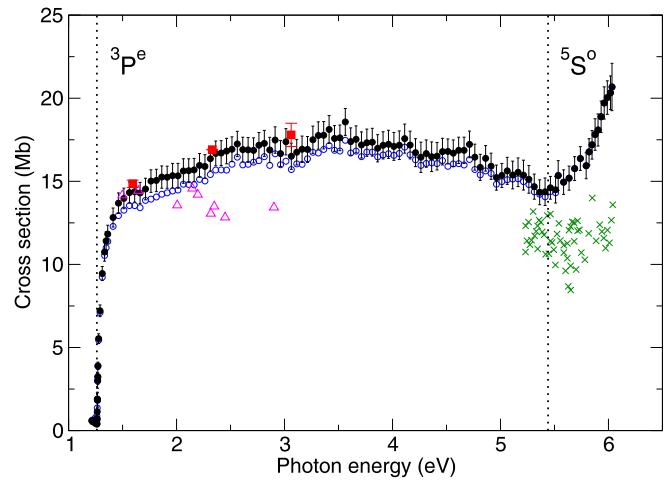

FIG. 3. Experimental cross sections for photodetachment of C$^-$($^4S^o$) as a function of the photon energy. Full circle: present work with a pulsed laser and correction for saturation; open circles: present work with a pulsed laser without correction for saturation; full square: present work with a continuous laser. Error bars for the pulsed laser correspond to one standard deviation as estimated by expression (8). Open triangles: Seman and Branscomb [4]; crosses: Haeffler et al. [31]. Vertical dotted lines: positions of the C(^3P) and C($^5S^o$) thresholds.

limited range of photon energies. Further discussion of their work can be found in the review by Andersen [2].

We first note that the cross section does not fall to zero below the photodetachment threshold of C$^-$($^4S^o$), which indicates that some anions are produced in the ^2D excited state. Several control measurements from threshold to a photon energy of 2.7 eV were conducted using the VMI spectrometer to determine the branching ratio between each channel. We found that the branching ratio is almost constant at 2% throughout the controlled range, except around 1.38 eV, just above threshold, where it reaches at most 4%. As this quantity depends on both the population and the cross section of each state entering the beam composition, the problem is not experimentally constrained. We will address this in future work, but some insight can be gained from the theoretical study by Zhou et al. [34], which suggests that the cross section for photodetachment of C$^-$(^2D) is of a similar order of magnitude to that for photodetachment of C$^-$($^4S^o$) over the energy range considered, with a small peak above the $^4S^o$ photodetachment threshold. This in turn suggests that the population of C$^-$(^2D) in our anion beam is very small and that the measured cross sections are relatively unaffected by the presence of this state. Even in the worst case, near threshold, the estimate of the error obtained by combining the measured branching ratio and the theoretical cross section is of the order of 1.5%, less than the experimental uncertainty.

Just above threshold, the cross section increases as $\sqrt{E}$, where E is the photoelectron energy, since the dominant channel is C($1s^2 2s^2 2p^2\ ^3P$) $+ e^-$($\ell = 0$). Beyond 1 eV, it increases slightly with photon energy before a small dip in the vicinity of the C($1s^2 2s 2p^3\ ^5S^o$) threshold, followed by a steep increase due to the opening of the C($^5S^o$) $+ e^-$($\ell = 1$) channel.

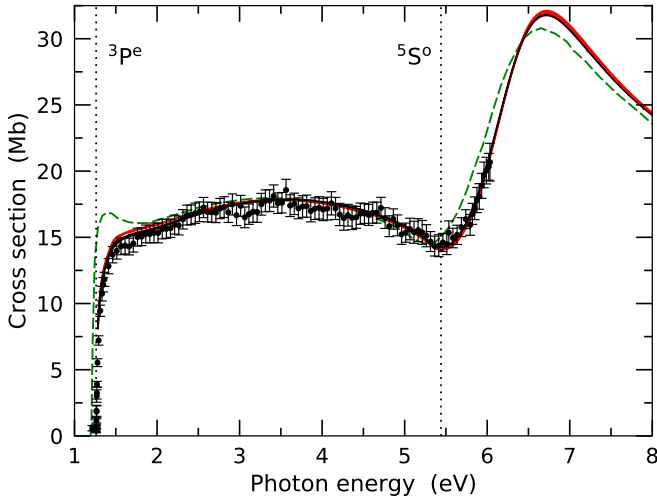FIG. 4. Experimental and theoretical photodetachment cross sections of $C^-(^4S^o)$ as a function of the photon energy. Full circles: present work with a pulsed laser and correction for saturation. Black full line: *R*-matrix method, length form; red full line: *R*-matrix method, velocity form; the thickness of the lines corresponds to the variation of results for different values of the calculation parameters (see text for details). Dashed line: Zhou *et al.* [7], length form. Vertical dotted lines: positions of the $C(^3P)$ and $C(^5S^o)$ thresholds.

In the wake of their pioneering work on the photodetachment of O^- [35,36], Seman and Branscomb [4] investigated C^- in the spectral region between 0.4 and 2.6 μm (0.478–3.1 eV). Their relative cross sections were normalized using the absolute values for O^- [36] in the photon energy region between 2 and 3 eV where the values of both sets of cross sections are relatively constant. The O^- cross sections were recently found to have been underestimated by about 20% and to be in fact slightly increasing with photon energy [3]. Renormalizing the data from [4] using the revised photodetachment cross section of O^- brings them into better agreement with our current results, except for the first two values at about 1.5 eV which are then too large.

The steep rise of the photodetachment cross section above the $C(^5S^o)$ threshold contrasts with the nearly constant behavior observed in this region by Haeffler *et al.* [31]. Their results were also normalized to the earlier photodetachment cross sections of O^- [36], but renormalization with the absolute values by Génévriez *et al.* [3] is inconclusive as the energy dependence is very different and the values are very dispersed.

We also note the very good agreement between our measurements using a continuous laser and using a pulsed laser taking into account the saturation effect, validating the developments leading to the correction coefficients of Fig. 2.

In Fig. 4, the current absolute cross sections for photodetachment of $C^-(^4S^o)$ are compared with the results of our *R*-matrix calculation and those by Zhou *et al.* [7]. Other theoretical studies undertaken before 2004 [37–39] have been thoroughly discussed in [2,7], and since the agreement with experiment tends to be less good, they are not reproduced here.

Both calculations are completely *ab initio*, all coupled angular momenta are included, and no energy shift was introduced. The radius a of the inner region is defined by the most diffuse atomic orbital, but as mentioned earlier, we have verified the stability of our results by performing calculations with different values of a from $25a_0$ to $35a_0$, varying the number of continuum orbitals between 25 and 50, obtaining electron affinities between 1.2575 and 1.2613 eV. The cross sections resulting from these parametric tests are summarized in Fig. 4 by the thickness of the lines corresponding to the current *R*-matrix calculations. More precisely, two curves following the largest and smallest values of the calculated cross sections are plotted, and the area between them is shaded. The differences between the cross sections obtained using the length and velocity representations of the dipole matrix are very small, less than 2% over the energy range considered, which is generally a good, but not sufficient, indication of the accuracy of a calculation.

The agreement between calculation and experiment is excellent over the whole range of energy covered by the experiment. The overall agreement with the results by Zhou *et al.* [7] is also very good. The main difference is in the region just above the first photodetachment threshold where our values for the total cross section, experimental and theoretical, increase monotonically, without the narrow peak due to a slightly larger contribution from the $C(1s^2 2s^2 2p^2\ ^3P) + e^-(\ell = 0)$ channel in the calculations of [7].

Since the objective of [7] was to study photodetachment from threshold up to 13 eV, only one orbital $(3d)$ was optimized on the polarizability of the carbon ground state, while the $3s$ and $3p$ orbitals correspond to spectroscopic orbitals for the $C(1s^2 2s^2 2p3s\ ^3P^o)$ and $C(1s^2 2s^2 2p3p\ ^3D)$ states. In our work, the $n = 3$ and the $4f$ orbitals are used to improve the energy of $C(1s^2 2s^2 2p^2\ ^3P)$, while the $4s$, $4p$, and $4d$ orbitals are optimized on its polarizability. The size of our *R*-matrix inner region $(a = 25\text{–}35a_0)$ is hence substantially larger than in the calculations by Zhou *et al.* $(a = 23.4a_0)$, but our computed cross sections remain stable with varying a. As a result, our calculations yield better values for the polarizability of the carbon ground state and for the electron affinity, as well as for the $^5S^o$ threshold. Part of the difference might also be due to the treatment of the outer region. However, in previous work on photodetachment of H^- [40] and O^- [11], for example, it was shown that for weak laser intensities, the perturbative approach of the UK APAP code gives results indistinguishable from those of the full *R*-matrix Floquet code [41,42] that includes a numerically very robust treatment of the outer region.

The total photodetachment cross section in Fig. 4 displays a broad plateau between 2.5 and 4.5 eV, then a minimum in the vicinity of the $^5S^o$ threshold followed by a broad maximum. The plateau is the result of a close balance between the $\ell = 0, 2$ partial wave contributions, which are shown in Fig. 5. The structure above the $^5S^o$ threshold is often referred to in the literature as a $1s^2 2s2p^4\ ^4P$ shape resonance (see, e.g., [7,39,43–45]). The dichotomic classification into shape resonances (open channel resonances occurring above a threshold) and Feshbach resonances (closed-channel resonances occurring below a threshold) is, however, not appropriate if electron correlations are strong and one-electron potential interaction models break down [43]. As shown in Fig. 5, the peak above the $C(^5S^o)$ threshold is, in fact, present even if this state is not included at all in the calculation. Figure 6 gives a
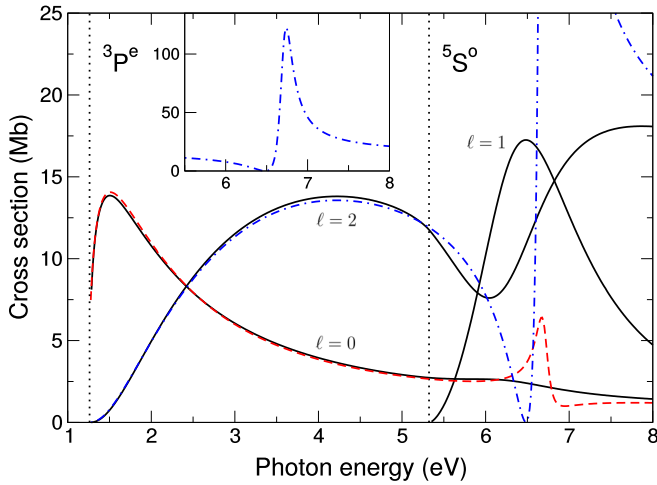
FIG. 5. Theoretical partial photodetachment cross sections as a function of the photon energy, length form. Full lines: full calculation, final channels $C(^3P) + e^-(\ell = 0, 2)$ and $C(^5S^o) + e^-(\ell = 1)$; dashed line: without $C(^5S^o)$, final channel $C(^3P) + e^-(\ell = 0)$; dashed-dotted line: without $C(^5S^o)$, final channel $C(^3P) + e-(\ell = 2)$. Vertical dotted lines: positions of the $C(^3P)$ and $C(^5S^o)$ thresholds in the R-matrix calculations.

schematic depiction of the different photodetachment pathways: direct photodetachment or excitation into a multiply excited $C^-(^4P)$ state embedded in the continuum, followed by autodetachment. The resonant state is represented by a shaded rectangular area centered on the resonance position, whose vertical extent indicates its width. When the $C(^5S^o)$ state is not included in the R-matrix basis expansion, the resonance is found at a higher energy with a greatly reduced width; in-
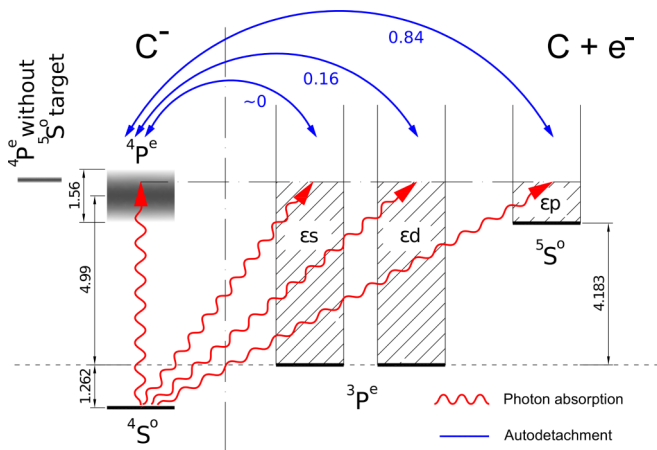

FIG. 6. Schematic representation of the photodetachment process involving an excited state of C^- embedded in three continua leading to the structure around 5.5 eV in the total cross section. The strong interaction between the $C^-(^4P)$ and $C(^5S^o)$ excited states greatly broadens and pushes down the $C^-(^4P)$ level, smoothing the resonance profile in the total cross section. The energy differences indicated are in eV. The shaded areas represent the positions and widths of the ^4P resonance in the calculations with and without the $C(^5S^o)$ state. The numbers below the arrows indicating the different autodetachment channels are the corresponding branching ratios.

cluding it shifts down and broadens the resonance. The strong interaction in the ^4P configuration space is thus responsible for the very broad resonance profile in the total cross section. This is reflected in the eigenvectors of the Hamiltonian of the R-matrix inner region: in the absence of the $C(^5S^o)$ state, there is an eigenvalue very close to the position of the resonance, characterized by weights of 46%, 14%, and 17% for the $1s^2 2s2p^4$, $1s^2 2s2p^3(^5S^o)3p$, and $1s^2 2s2p^3(^5S^o)4p$ bound configurations, respectively; the remaining 23% is distributed into more excited configurations. When the $C(^5S^o)$ state is included in the calculation, the eigenvector of the R-matrix inner region Hamiltonian associated with the resonance has a weight of only 18% in the $1s^2 2s2p^4$ configuration, 16% in $1s^2 2s2p^3(^5S^o)4p$, and 7% in $1s^2 2s2p^3(^5S^o)3p$. The other components are mainly those formed by $C(^5S^o)$ coupled to an R-matrix continuum p orbital.

An efficient way of analyzing resonances is to use the time-delay or lifetime matrix of the corresponding electron-carbon scattering problem: even broad resonances relatively close to threshold with a strong energy-dependent background and overlapping resonances can be fitted to Lorentzian functions whose position and height correspond, respectively, to the energy and lifetime of the resonances [46,47]. When the $^5S^o$ threshold is omitted from the calculation, the resonance occurs at $E_{res} = 5.457$ eV above the $C(^3P)$ threshold, with a width $\Gamma = 0.177$ eV. In our full calculations, the resonance position is $E_{res} = 4.99$ eV above the $C(^3P)$ threshold, corresponding to a photon energy of 6.25 eV, with a width of $\Gamma = 1.56$ eV. Furthermore, the probability of decay into a particular open channel (autodetachment; see Fig. 6) is given by the square of the modulus of the corresponding element in the eigenvector associated with the largest eigenvalue of the lifetime matrix. Using this, we find that the probability of the resonance to decay into the $C(^3P) + e^-(\ell = 0)$ channel is negligible, while the probability of decaying into the $C(^3P) + e^-(\ell = 2)$ or $C(^5S^o) + e^-(\ell = 1)$ channels are 0.16 and 0.84, respectively.

B. Asymmetry parameter

In Fig. 7, we present the values of the asymmetry parameter β from our experiment and our R-matrix calculations, and compare them with those from earlier work [7,32,33,48].

Close to threshold, the dominant detachment channel corresponds to a photoelectron in the spherically isotropic $\ell = 0$ wave, so that $\beta \approx 0$. It decreases to nearly the smallest possible value, -1, at about 2 eV before increasing again to $\beta \approx 0$. This general trend is similar to that for the photodetachment of O^- and reflects the interference between the $\ell = 0$ and $\ell = 2$ outgoing waves. The agreement with the few existing experimental data by Hall and Siegel [32], Calabrese et al. [48], and Brandon et al. [33] is very good. The agreement with the R-matrix calculations is also excellent over the whole range of photon energies considered. The small difference in the region of the minimum at 2 eV with the calculation by Zhou et al. [7] reflects the differences at low energies in the $\ell = 0$ and $\ell = 2$ partial cross sections shown in Fig. 5. Above the $C(1s^2 2s2p^3 \, ^5S^o)$ threshold, the $\ell = 1$ channel gives a constant contribution of $\beta = 2$, and is therefore not shown in Fig. 7. As in the calculations by Zhou et al. [7], the asymmetry parameter displays a dip above the $^5S^o$ threshold; in our work, this
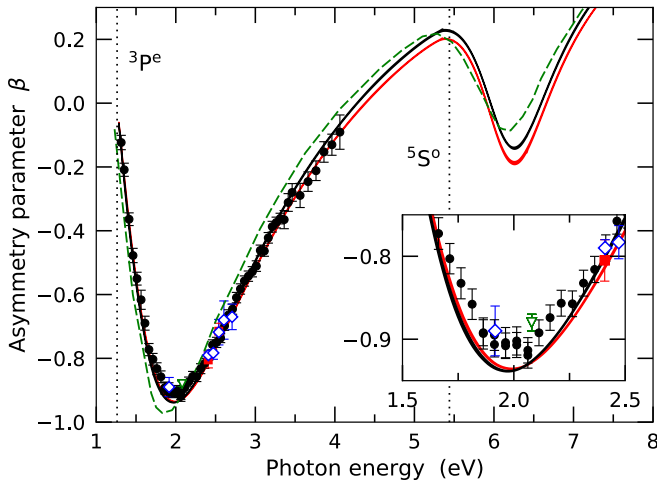
FIG. 7. Asymmetry parameter β for the photodetachment of C($^4S^o$). Experiment: circles, present measurements; full square, Hall *et al.* [32]; open lozenge, Calabrese *et al.* [48]; open triangle down, Brandon *et al.* [33]. Theory: black full line: current *R*-matrix results, length form; red full line: current *R*-matrix results, velocity form; the thickness of the lines corresponds to the variation of results for different values of the calculation parameters (see text for details); dashed line: Zhou *et al.* [7], length form. Vertical dotted lines: positions of the C(^3P) and C($^5S^o$) thresholds.

dip is slightly deeper and occurs at a slightly higher energy than in [7].

V. CONCLUSION

Using the animated crossed beam technique, we have measured absolute cross sections for the photodetachment of the ground state of carbon anion in the ground state, C$^-$($^4S^o$), for photon energies ranging from threshold up to 6 eV. As the peak intensity of the laser is high enough to provoke saturation in neutral production, a correction factor has been estimated at the cost of introducing further assumptions about the laser beam profile. We have verified that the corrected cross sections are in excellent agreement with the uncorrected absolute cross sections obtained using the ACB technique with continuous lasers, for which saturation does not occur. We note that the relative cross sections by Seman and Branscomb [4], renormalized using the absolute cross sections for O$^-$ by Génévriez *et al.* [3], tend to be in much better agreement with our measurements and the best available theoretical predictions.

By analyzing the images formed by the photoelectrons extracted from the interaction chamber through a velocity map imaging spectrometer, we have also determined the asymmetry parameters for photon energies from threshold up to

4 eV. The results are in excellent agreement with the few data available from previous measurements [32,33,48].

The experimental study has been completed by a set of *R*-matrix calculations including orbitals and pseudo-orbitals optimized using the CIVPOL computer code to reproduce accurate values of electron affinity and polarizability of the carbon ground state in an *ab initio* way. The photodetachment cross sections in length and velocity representations are very similar, satisfying a necessary criterion of convergence of the calculations. Our results are in excellent agreement with the measured absolute cross sections up to 6 eV, and are also very close to the values determined by Zhou *et al.* [7] who used the *R*-matrix method with the variable phase method to treat the outer region. Our experiment and calculations, however, do not reproduce the peak just above threshold obtained by Zhou *et al.* The photon energy range covered by our calculations extends up to 8 eV, which might be somewhat high considering the absence of excited states in our basis beyond C($1s^2 2s 2p^3\ ^5S^o$). Our results are, however, in excellent agreement with the values by Zhou *et al.* who included seven more threshold states [7] up to nearly 11 eV, which indicates that our calculations are converged over the whole range considered. The theoretical asymmetry parameters are also in excellent agreement with the experimental data.

Between the C($^5S^o$) threshold and 8 eV, the photodetachment cross section presents a broad peak which has often been qualified as a ^4P shape resonance with a configuration $1s^2 2s 2p^4$ or $1s^2 2s 2p^3 \bar{n}p$. We have shown that this resonance appears even in the absence of the C($^5S^o$) threshold, albeit with a much narrower width, provided excitations of at least two electrons from the ground configuration are taken into account. When the C($^5S^o$) threshold is included, continuum orbital configurations of the form $1s^2 2s 2p^3 (^5S^o)\epsilon p$ contribute to nearly 60% of the resonance wave function. These characteristics are a reminder of the importance of correlation effects in open-shell systems which break the convenient system of classification of resonances based on electron in a potential approximation.

A more detailed study of the photodetachment of the excited C$^-$(^2D) anion should also be performed in order to verify that its contribution to the measured signal in the current experiment is indeed negligible. It would be interesting to extend the range of photon energies in order to investigate experimentally resonances at higher energies, not just for C$^-$ but also in heavier systems such as Si$^-$, but this requires the use of different light sources.

[1] L. M. Branscomb and B. E. J. Pagel, Mon. Not. R. Astron. Soc. **118**, 258 (1958).

[2] T. Andersen, Phys. Rep. **394**, 157 (2004).

[3] M. Génévriez, K. M. Dunseath, M. Terao-Dunseath, A. Hibbert, A. Dochain, R. Marion, and X. Urbain, Phys. Rev. A **98**, 033410 (2018).

[4] M. L. Seman and L. M. Branscomb, Phys. Rev. **125**, 1602 (1962).

[5] D. Bresteau, C. Drag, and C. Blondel, Phys. Rev. A **93**, 013414 (2016).

[6] D. Feldmann, Chem. Phys. Lett. **47**, 338 (1977).

[7] H. L. Zhou, S. T. Manson, A. Hibbert, L.V. Ky, N. Feautrier, and J.-C. Chang, Phys. Rev. A **70**, 022713 (2004).

[8] N. D. Gibson, C. W. Walter, O. Zatsarinny, T. W. Gorczyca, G. D. Akerman, J. D. Bozek, M. Martins, B. M. McLaughlin, and N. Berrah, Phys. Rev. A **67**, 030703(R) (2003).

[9] A. Perry-Sassmannshausen, T. Buhr, A. Borovik, M. Martins, S. Reinwardt, S. Ricz, S. O. Stock, F. Trinter, A. Müller, S. Fritzsche, and S. Schippers, Phys. Rev. Lett. **124**, 083203 (2020).

[10] P. Defrance, F. Brouillard, W. Claeys, and G. V. Wassenhove, J. Phys. B: At. Mol. Phys. **14**, 103 (1981).

[11] M. Génévriez, X. Urbain, A. Dochain, A. Cyr, K. M. Dunseath, and M. Terao-Dunseath, Phys. Rev. A **94**, 023407 (2016).

[12] I. León, Z. Yang, H.-T. Liu, and L.-S. Wang, Rev. Sci. Instrum. **85**, 083106 (2014).

[13] C. J. Johnson, B. B. Shen, B. L. J. Poad, and R. E. Continetti, Rev. Sci. Instrum. **82**, 105105 (2011).

[14] X. Urbain, D. Bech, J.-P. Van Roy, M. Géléoc, S. J. Weber, A. Huetz, and Y. J. Picard, Rev. Sci. Instrum. **86**, 023305 (2015).

[15] P. Defrance, J. Lecointre, and R. Janev, in *Atomic and Plasma-Material Interaction Data for Fusion* (IAEA, Vienna, 2014), Vol. 16.

[16] A. Muller, K. Huber, K. Tinschert, R. Becker, and E. Salzborn, J. Phys. B **18**, 2993 (1985).

[17] G. A. Alna'washi, K. K. Baral, N. B. Aryal, C. M. Thomas, and R. A. Phaneuf, J. Phys. B **47**, 105201 (2014).

[18] P. Defrance, W. Claeys, A. Cornet, and G. Poulaert, J. Phys. B **14**, 111 (1981).

[19] M. Génévriez, J. J. Jureta, P. Defrance, and X. Urbain, Phys. Rev. A **96**, 010701(R) (2017).

[20] M. Génévriez and X. Urbain, Phys. Rev. A **91**, 033403 (2015).

[21] A. T. J. B. Eppink and D. H. Parker, Rev. Sci. Instrum. **68**, 3477 (1997).

[22] B. Dick, Phys. Chem. Chem. Phys. **16**, 570 (2014).

[23] JCGM 100: Evaluation of Measurement Data – Guide to the Expression of Uncertainty in Measurement (Joint Committee for Guides in Metrology, 2008).

[24] http://www.apap-network.org/.

[25] E. P. Wigner and L. Eisenbud, Phys. Rev. **72**, 29 (1947).

[26] P. G. Burke, *R-matrix Theory of Atomic Collisions: Application to Atomic, Molecular and Optical Processes*, Springer Series on Atomic, Optical, and Plasma Physics, Vol. 61 (Springer, Berlin, 2011).

[27] E. Clementi and C. Roetti, At. Data Nucl. Data Tables **14**, 177 (1974).

[28] V. K. Lan, M. Le Dourneuf, and P. G. Burke, J. Phys. B: At. Mol. Phys. **9**, 1065 (1976).

[29] A. Kramida, Y. Ralchenko, J. Reader, and NIST ASD Team (2020). NIST Atomic Spectra Database (version 5.8), https://physics.nist.gov/asd.

[30] A. K. Das and A. J. Thakkar, J. Phys. B: At., Mol. Opt. Phys. **31**, 2215 (1998).

[31] G. Haeffler, D. Hanstorp, I. Y. Kiyan, U. Ljungblad, H. H. Andersen, and T. Andersen, J. Phys. B: At., Mol. Opt. Phys. **29**, 3017 (1996).

[32] J. L. Hall and M. W. Siegel, J. Chem. Phys. **48**, 943 (1968).

[33] W. D. Brandon, D. H. Lee, D. Hanstorp, and D. J. Pegg, J. Phys. B: At., Mol. Opt. Phys. **31**, 751 (1998).

[34] H.-L. Zhou, S. T. Manson, A. Hibbert, L. Vo Ky, and N. Feautrier, Phys. Rev. A **72**, 032723 (2005).

[35] L. M. Branscomb, D. S. Burch, S. J. Smith, and S. Geltman, Phys. Rev. **111**, 504 (1958).

[36] S. J. Smith and L. M. Branscomb, Rev. Sci. Instrum. **31**, 733 (1960).

[37] G. F. Gribakin, A. A. Gribakina, B. V. Gul'tsev, and V. K. Ivanov, J. Phys. B: At., Mol. Opt. Phys. **25**, 1757 (1992).

[38] C. A. Ramsbottom, K. L. Bell, and K. A. Berrington, J. Phys. B: At. Mol. Phys. **26**, 4399 (1993).

[39] N. Miura, T. Noro, and F. Sasaki, J. Phys. B: At., Mol. Opt. Phys. **30**, 5419 (1997).

[40] M. Dorr, J. Purvis, M. Terao-Dunseath, P. G. Burke, C. J. Joachain, and C. J. Noble, J. Phys. B: At., Mol. Opt. Phys. **28**, 4481 (1995).

[41] P. G. Burke, P. Francken, and C. J. Joachain, J. Phys. B: At., Mol. Opt. Phys. **24**, 761 (1991).

[42] M. Dorr, M. Terao-Dunseath, J. Purvis, C. J. Noble, P. G. Burke, and C. J. Joachain, J. Phys. B: At., Mol. Opt. Phys. **25**, 2809 (1992).

[43] S. J. Buckman and C. W. Clark, Rev. Mod. Phys. **66**, 539 (1994).

[44] G. Y. Kashenock and V. K. Ivanov, Phys. Lett. A **245**, 110 (1998).

[45] O. Zatsarinny, K. Bartschat, L. Bandurina, and V. Gedeon, Phys. Rev. A **71**, 042702 (2005).

[46] F. T. Smith, Phys. Rev. **118**, 349 (1960).

[47] K. M. Dunseath, M. Terao-Dunseath, and J.-M. Launay, J. Phys. B: At., Mol. Opt. Phys. **33**, 3037 (2000).

[48] D. Calabrese, A. M. Covington, D. L. Carpenter, J. S. Thompson, T. J. Kvale, and R. Collier, J. Phys. B: At., Mol. Opt. Phys. **30**, 4791 (1997).